

Infrared to terahertz optical conductivity of *n*-type and *p*-type monolayer MoS₂ in the presence of Rashba spin-orbit coupling

Y. M. Xiao,^{1,2,*} W. Xu,^{1,3,†} B. Van Duppen,^{2,‡} and F. M. Peeters^{2,§}

¹*Department of Physics and Astronomy and Yunnan Key Laboratory for Micro/Nano Materials and Technology, Yunnan University, Kunming 650091, China*

²*Department of Physics, University of Antwerp, Groenenborgerlaan 171, B-2020 Antwerpen, Belgium*

³*Key Laboratory of Materials Physics, Institute of Solid State Physics, Chinese Academy of Sciences, Hefei 230031, China*

(Received 14 July 2016; revised manuscript received 21 September 2016; published 18 October 2016)

We investigate the effect of Rashba spin-orbit coupling (SOC) on the optoelectronic properties of *n*- and *p*-type monolayer MoS₂. The optical conductivity is calculated within the Kubo formalism. We find that the spin-flip transitions enabled by the Rashba SOC result in a wide absorption window in the optical spectrum. Furthermore, we evaluate the effects of the polarization direction of the radiation, temperature, carrier density, and the strength of the Rashba spin-orbit parameter on the optical conductivity. We find that the position, width, and shape of the absorption peak or absorption window can be tuned by varying these parameters. This study shows that monolayer MoS₂ can be a promising tunable optical and optoelectronic material that is active in the infrared to terahertz spectral range.

DOI: [10.1103/PhysRevB.94.155432](https://doi.org/10.1103/PhysRevB.94.155432)

I. INTRODUCTION

The discovery of atomically thin two-dimensional (2D) materials has created a completely new field of research. These materials are promising for applications in next generation of high-performance nanoelectronics devices [1]. Recently, new types of 2D materials such as monolayer transition metal dichalcogenides MX₂ (M = Mo, W, Nb, Ta, Ti, and X = S, Se, Te) have been synthesized. These 2D materials are formed by layered structures in the form of X-M-X with the chalcogen atoms in two hexagonal planes separated by a plane of metal atoms [2–4]. Transition metal dichalcogenides (TMDCs) have a sizable band gap that can change from indirect in multilayers to direct in a single-layer structure [2]. For example, molybdenum disulfide (MoS₂) shows a transition from an indirect band gap of 1.29 eV in bulk to a direct band gap near 1.90 eV in its monolayer form at the inequivalent high-symmetry K and K' points [3,5].

Since its first isolation, monolayer MoS₂ [3,6] has been investigated intensively because it exhibits interesting and important electronic and optical properties. Very recently, one has demonstrated that monolayer MoS₂ (ML-MoS₂) based field-effect transistors (FETs) can have room-temperature on/off ratios of the order of 10⁸ and can exhibit a carrier mobility larger than 200 cm²/(V s) [7–9]. Other MoS₂ based electronic components such as gas sensors [10], phototransistors, photodetectors with high responsivity [11], and even LEDs [12] have been realized experimentally. Currently, the investigation of ML-MoS₂ has become a fast-growing field of research with great potential for electronics, optics, and optoelectronics.

The electronic band structure for ML-MoS₂ can be calculated in a $\mathbf{k} \cdot \mathbf{p}$ theory framework [13,14]. Unlike massless Dirac fermions in graphene, the electronic states in monolayer

TMDCs (ML-TMDCs) can be described as massive Dirac fermions. Furthermore, it was found that there exists an intrinsic spin-orbit coupling (SOC) in ML-MoS₂, which gives rise to a splitting of the conduction and valence bands with opposite spin orientations [13,15]. In a recent work, Li *et al.* [16] calculated the optical conductivity in ML-MoS₂ in the visible range as determined by the interband optical transitions from the valence to the conduction bands. The collective excitations of ML-MoS₂, e.g., plasmons, and screening have also been examined and discussed [17]. The presence of a strong intrinsic SOC that couples between spin and valley degrees of freedom has led to the proposal that the TMDCs can be interesting materials for valleytronics and spintronics [18–21].

The control of carrier spin dynamics in semiconductor nanostructures is a key issue in spintronics and it can be achieved through the electrical manipulation of the SOC induced by the Rashba effect [22–24]. The investigation of optical properties such as collective excitations [25,26] and optical conductivities [27–30] has been conducted and show how the Rashba effect affects the optical properties of traditional 2D semiconductor based spintronic devices. This indicates that the Rashba effect has a strong influence on the plasmon modes and low-frequency optical spectrum.

When an electric field is applied perpendicular to a ML-MoS₂ flake, inversion symmetry is broken and, according to the Kane-Mele model [31], a Rashba SOC term is added to the Hamiltonian. As a consequence, spin \hat{s}_z is no longer a good quantum number [31–33] and it becomes possible to have transitions between spin-split electronic states. This enables the observation of spin-related optical phenomena that were found before to be presented in traditional 2D electron gasses (2DEGs) [25–30]. In ML-MoS₂, there is a combination of both spin-coupling mechanisms with which one can expect to realize interesting spin-optics effects. Moreover, thanks to the tunability of the Rashba SOC with the external electric field, it is possible to turn these effects on and off. Alternatively, one could also deposit various atoms on the MoS₂ surface that can enhance the Rashba SOC as has been demonstrated in gold-doped graphene [34] and Bi₂Se₃(001) surfaces [35].

*yiming.xiao@uantwerpen.be

†wenxu_issp@aliyun.com

‡ben.vanduppen@uantwerpen.be

§francois.peeters@uantwerpen.be

The effects of the Rashba SOC on the optical properties of graphene have been studied [36–39]. It shows that the Rashba effect strongly affects the optical properties of graphene. In the presence of the Rashba SOC, the optical conductivity of graphene features absorption peaks and kinks which are due to interband transitions between the spin-split states [38,39]. ML-MoS₂ has a low-energy parabolic band which is different from the linear dispersion relation of graphene. In order to understand the ML-MoS₂ material systems more deeply and to explore their further applications in practical devices working in the low-energy bandwidth, it is necessary to examine the roles played by the Rashba SOC in affecting the optoelectronic properties.

Along with numerous theoretical studies, the optical and transport properties of MoS₂ have also been experimentally investigated [3,5,7–9,19–21]. However, most of these works focus on the optoelectronic properties induced by interband transitions between the conduction and valence bands that lie in the visible range of the electromagnetic (EM) spectrum. In this article, we predict that the Rashba effect induces spin-flip transitions that can have a great impact on the optoelectronic response of ML-MoS₂ in the infrared to terahertz range. To the best of our knowledge, very little research has been reported on the optoelectronic properties of ML-MoS₂ in this range of the light spectrum. In this regime, the intrinsic and Rashba SOC can play an important role in determining the optoelectronic response. We intend to study the optical conductivity of ML-MoS₂ in the presence of the Rashba SOC under linear and circular polarized radiation field. By calculating the different contributions of intraband and interband electronic transitions, we examine the effects of *n*- and *p*-type doping (for varying carrier density via chemical doping or applying a gate voltage), temperature, and the Rashba SOC strength on the optical conductivity of ML-MoS₂. We calculate the electronic band structure of ML-MoS₂ starting from a 4 × 4 matrix Hamiltonian with the addition of the Kane-Mele Rashba SOC.

The present paper is organized as follows. In Sec. II, we describe the band structure and solve for the single-particle states of ML-MoS₂ in the presence of the Rashba effect. The absorptive part of the optical conductivity is evaluated through the standard Kubo formalism in the presence of a linearly and/or circularly polarized radiation field in Sec. III. The optical transition channels for different doping types and doping levels and the results for the absorptive part of the optical conductivity are presented and discussed in Sec. IV. Our main conclusions are summarized in Sec. V.

II. ELECTRONIC BAND STRUCTURE

In this study we consider a ML-MoS₂ in the *xy* plane on top of a dielectric wafer such as SiO₂ [40,41]. The effective $\mathbf{k} \cdot \mathbf{p}$ Hamiltonian for a charge carrier (an electron or a hole) in the low-energy regime near the K (K') point in ML-MoS₂ in the presence of the Rashba SOC can be written as [13,15,16,32,33]

$$\hat{H}^\zeta = \left[at(\zeta k_x \hat{\sigma}_x + k_y \hat{\sigma}_y) + \frac{\Delta}{2} \hat{\sigma}_z \right] \otimes \hat{I} + \zeta \gamma_v \frac{\hat{I} - \hat{\sigma}_z}{2} \otimes \hat{s}_z + \gamma_R (\zeta \hat{\sigma}_x \otimes \hat{s}_y - \hat{\sigma}_y \otimes \hat{s}_x), \quad (1)$$

where $\hat{\sigma}_i$ and \hat{s}_i are the Pauli matrices of the sublattice pseudospin and the real spin, respectively. \hat{I} is the 2 × 2 unit matrix and the valley index $\zeta = \pm$ refers to the K (K') valley. This Hamiltonian reads in the basis $\Psi^+ = \{\psi_{A\uparrow}, \psi_{A\downarrow}, \psi_{B\uparrow}, \psi_{B\downarrow}\}^T$ and $\Psi^- = \{\psi_{A\downarrow}, \psi_{A\uparrow}, \psi_{B\downarrow}, \psi_{B\uparrow}\}^T$ for both valleys explicitly as

$$\hat{H}^\zeta = \begin{pmatrix} \Delta/2 & 0 & \zeta atk_{-\zeta} & 0 \\ 0 & \Delta/2 & 2i\gamma_R & \zeta atk_{-\zeta} \\ \zeta atk_\zeta & -2i\gamma_R & \gamma_v - \Delta/2 & 0 \\ 0 & \zeta atk_\zeta & 0 & -\gamma_v - \Delta/2 \end{pmatrix}, \quad (2)$$

where $\mathbf{k} = (k_x, k_y)$ is the wave vector, $k_\pm = k_x \pm ik_y$, $a = 3.193 \text{ \AA}$ is the lattice parameter, $t = 1.1 \text{ eV}$ is the hopping parameter [13], the intrinsic SOC parameter $2\gamma_v = 150 \text{ meV}$ is the spin splitting at the top of the valence band in the absence of the Rashba SOC [13,42], $\Delta = 1.66 \text{ eV}$ is the direct band gap between the valence and conduction band used in our calculation [13,15,16], and γ_R is the Rashba SOC parameter which can be tuned via an electrical field and can be determined by *ab initio* calculation or by fitting with experimental data. Kormányos *et al.* [43] estimated the value of the Rashba parameter for ML-MoS₂ as $\alpha_R = 0.033 \text{ e\AA}^2 E_z [\text{V/\AA}]$ for a spin-split two-band model which corresponds to $\gamma_R = 0.0078 \text{ e\AA} E_z [\text{V/\AA}]$ in our model with the relation of $\gamma_R = \alpha_R \Delta / (2at)$ obtained in Ref. [44] where E_z is the perpendicular electric field. We would like to point out that the Rashba effect can not only be tuned by a gate voltage but can also be enhanced by adatoms as has been realized in graphene [34]. For example, a large Rashba parameter 72 meV is found in monolayer MoTe₂ on a EuO substrate [45].

From the above Hamiltonian, we can describe the spin states in both conduction and valence bands in the presence of the Rashba effect. The corresponding Schrödinger equation for ML-MoS₂ near the valley K (K') can be solved analytically and the eigenvalues are the solutions of the diagonalized equation

$$\varepsilon^4 - A_2 \varepsilon^2 + A_1 \varepsilon + A_0 = 0, \quad (3)$$

where

$$A_0 = (\Delta^2/4 + a^2 t^2 k^2)^2 + \gamma_R^2 \Delta (\Delta + 2\gamma_v) - \Delta^2 \gamma_v^2 / 4,$$

$$A_1 = \Delta \gamma_v^2 - 4\gamma_v \gamma_R^2,$$

and

$$A_2 = \Delta^2/2 + 2a^2 t^2 k^2 + 4\gamma_R^2 + \gamma_v^2.$$

The energy dispersion $\varepsilon_{\mathbf{k},\xi} = \varepsilon_{\mathbf{k},\lambda\nu}$ can be obtained through solving Eq. (3) analytically with the general solution of a quartic equation [46]. Here, we defined the total quantum number $\xi = (\zeta, \lambda, s)$, where $\lambda = \pm$ refers to the conduction/valence band and $s = \pm$ is the spin index and ζ labels the valley. We often use the quantity $\nu = \zeta s = \pm$ to exploit the valley/spin symmetry of the system.

The corresponding eigenfunction for a state near the K (K') point is

$$|\mathbf{k}, \xi\rangle = \psi_\xi(\mathbf{k}, \mathbf{r}) = \mathcal{N}_{\lambda\nu}(k) [c_1^\xi, c_2^\xi, c_3^\xi, c_4^\xi] e^{i\mathbf{k}\cdot\mathbf{r}}. \quad (4)$$

Equation (4) is expressed in the form of a row vector where the values of the eigenfunction elements are

$$\begin{aligned} c_1^\xi &= -2i\gamma_R a^2 t^2 k_{-z}^2, & c_2^\xi &= \varsigma a t k_{-z} b_1^{\lambda\nu}, \\ c_3^\xi &= -2i\varsigma \gamma_R a t k_{-z} b_0^{\lambda\nu}, & c_4^\xi &= b_0^{\lambda\nu} b_2^{\lambda\nu}, \end{aligned}$$

with

$$\begin{aligned} b_1^{\lambda\nu} &= \varepsilon_{\mathbf{k},\lambda\nu}^2 - \gamma_v \varepsilon_{\mathbf{k},\lambda\nu} + \Delta(2\gamma_v - \Delta)/4 - a^2 t^2 k^2, \\ b_2^{\lambda\nu} &= b_1^{\lambda\nu} - 4\gamma_R^2, & b_0^{\lambda\nu} &= \varepsilon_{\mathbf{k},\lambda\nu} - \Delta/2. \end{aligned}$$

The normalization coefficient $\mathcal{N}_{\lambda\nu}(k)$ can be written as

$$\mathcal{N}_{\lambda\nu}(k) = 1/\sqrt{\hbar^{\lambda\nu}}, \quad (5)$$

with $\hbar^{\lambda\nu} = 4\gamma_R^2 a^2 t^2 k^2 [a^2 t^2 k^2 + (b_0^{\lambda\nu})^2] + a^2 t^2 k^2 (b_1^{\lambda\nu})^2 + (b_0^{\lambda\nu} b_2^{\lambda\nu})^2$.

III. OPTICAL CONDUCTIVITY

In the present study, we evaluate the optical conductivity in ML-MoS₂ using the standard Kubo formula [47,48]

$$\sigma_{\alpha\beta}(\mathbf{q}, \omega) = i \frac{e^2 n_i}{m\omega} \delta_{\alpha\beta} + \frac{1}{\omega} \int_0^\infty dt e^{i\tilde{\omega}t} \langle [j_\alpha^\dagger(\mathbf{q}, t), j_\beta(\mathbf{q}, 0)] \rangle, \quad (6)$$

where $(\alpha, \beta) = (x, y)$ for a 2D system, $j_\alpha(\mathbf{q}, t)$ is the current density operator, $\tilde{\omega} = \omega + i\eta$ ($\eta \rightarrow 0^+$), and n_i is the carrier density for electrons in the conduction band or holes in the valence band. It should be noted that the first term in Eq. (6) is the diamagnetic term [48]. In this paper we concentrate on calculating the real part of the optical conductivity, where this term does not contribute because it is purely imaginary at nonzero frequencies.

In the optical limit of $\mathbf{q} \rightarrow 0$, the dynamical optical conductivity for the ML-MoS₂ system at an incident photon frequency ω can be written in the Kubo-Greenwood form as [48,49]

$$\begin{aligned} \sigma_{\alpha\beta}(\omega) &= \frac{ie^2}{\omega} \sum_{\xi', \xi} \sum_{\mathbf{k}', \mathbf{k}} \langle \mathbf{k}, \xi | \hat{v}_\alpha^\xi | \mathbf{k}', \xi' \rangle \langle \mathbf{k}', \xi' | \hat{v}_\beta^\xi | \mathbf{k}, \xi \rangle \\ &\times \frac{f(\varepsilon_{\mathbf{k}, \xi}) - f(\varepsilon_{\mathbf{k}', \xi'})}{\varepsilon_{\mathbf{k}, \xi} - \varepsilon_{\mathbf{k}', \xi'} + \hbar(\omega + i\eta)}, \end{aligned} \quad (7)$$

where the velocity operator $\hat{v}_\alpha^\xi = \hbar^{-1} \partial \hat{H}^\xi / \partial k_\alpha$, $\eta = \tau^{-1}$, τ is the transport relaxation time, and $f(\varepsilon_{\mathbf{k}, \xi}) = f(\varepsilon_{\mathbf{k}, \lambda\nu}) = \{\exp[(\varepsilon_{\mathbf{k}, \lambda\nu} - \mu_\lambda)/(k_B T)] + 1\}^{-1}$ is the Fermi-Dirac distribution function with μ_λ the chemical potential for electrons or holes and the temperature T . It should be noted that we use a constant relaxation time for the following calculations where the specific scattering events are not considered. Very recently, the intraband optical conductivity for ML-MoS₂ has also been calculated [50], and the evaluation of the relaxation time by impurity scattering had been discussed in Ref. [51]. The longitudinal optical conductivity at valley ς can be written as

$$\begin{aligned} \sigma_{xx}^\varsigma(\omega) &= \frac{ie^2}{\omega} \sum_{\lambda'v', \lambda\nu} \sum_{\mathbf{k}', \mathbf{k}} w_{\lambda'v', \lambda\nu}^{xx}(\mathbf{k}', \mathbf{k}) \\ &\times \frac{f(\varepsilon_{\mathbf{k}, \lambda\nu}) - f(\varepsilon_{\mathbf{k}', \lambda'v'})}{\varepsilon_{\mathbf{k}, \lambda\nu} - \varepsilon_{\mathbf{k}', \lambda'v'} + \hbar(\omega + i\eta)}, \end{aligned} \quad (8)$$

where

$$w_{\lambda'v', \lambda\nu}^{xx}(\mathbf{k}', \mathbf{k}) = \frac{a^4 t^4 k^2 [p^2 + r^2 + 2pr \cos(2\phi)]}{\hbar^2 \hbar^{\lambda\nu} \hbar^{\lambda'v'}} \delta_{\mathbf{k}, \mathbf{k}'},$$

with

$$\begin{aligned} p &= b_0^{\lambda'v'} (4\gamma_R^2 a^2 t^2 k^2 + b_1^{\lambda\nu} b_2^{\lambda'v'}), \\ r &= b_0^{\lambda\nu} (4\gamma_R^2 a^2 t^2 k^2 + b_1^{\lambda'v'} b_2^{\lambda\nu}). \end{aligned}$$

Moreover, the transverse or ‘‘Hall’’ optical conductivity at valley ς is

$$\begin{aligned} \sigma_{xy}^\varsigma(\omega) &= \frac{ie^2}{\omega} \sum_{\lambda'v', \lambda\nu} \sum_{\mathbf{k}', \mathbf{k}} w_{\lambda'v', \lambda\nu}^{xy, \varsigma}(\mathbf{k}', \mathbf{k}) \\ &\times \frac{f(\varepsilon_{\mathbf{k}, \lambda\nu}) - f(\varepsilon_{\mathbf{k}', \lambda'v'})}{\varepsilon_{\mathbf{k}, \lambda\nu} - \varepsilon_{\mathbf{k}', \lambda'v'} + \hbar(\omega + i\eta)}, \end{aligned} \quad (9)$$

where

$$w_{\lambda'v', \lambda\nu}^{xy, \varsigma}(\mathbf{k}', \mathbf{k}) = \frac{a^4 t^4 k^2 i(p^2 - r^2) + 2\varsigma pr \sin(2\phi)}{\hbar^2 \hbar^{\lambda\nu} \hbar^{\lambda'v'}} \delta_{\mathbf{k}, \mathbf{k}'},$$

The $\eta \rightarrow 0^+$ limit in the above equations can be divided into a principal-value (\mathcal{P}) part and a Dirac-delta part through the Dirac identity

$$\lim_{\eta \rightarrow 0^+} \frac{1}{x + i\eta} = \mathcal{P} \left(\frac{1}{x} \right) - i\pi \delta(x). \quad (10)$$

Thus, the optical conductivity can be separated into real and imaginary parts. The real part of the longitudinal optical conductivity and the imaginary part of the Hall optical conductivity at valley ς take respectively the forms

$$\text{Re } \sigma_{xx}^\varsigma(\omega) = \sum_{\lambda'v', \lambda\nu} \text{Re } \sigma_{xx, \varsigma}^{\lambda\nu\lambda'v'}(\omega), \quad (11)$$

with

$$\begin{aligned} \text{Re } \sigma_{xx, \varsigma}^{\lambda\nu\lambda'v'}(\omega) &= \int_0^\infty dk \frac{e^2 a^4 t^4 k^3 (p^2 + r^2)}{2\hbar^3 \omega \hbar^{\lambda\nu} \hbar^{\lambda'v'}} \\ &\times [f(\varepsilon_{k, \lambda\nu}) - f(\varepsilon_{k, \lambda\nu} + \hbar\omega)] \\ &\times \delta[\omega - \omega_{\lambda\nu}^{\lambda'v'}(k)], \end{aligned}$$

and

$$\text{Im } \sigma_{xy}^\varsigma(\omega) = \sum_{\lambda'v', \lambda\nu} \text{Im } \sigma_{xy, \varsigma}^{\lambda\nu\lambda'v'}(\omega), \quad (12)$$

with

$$\begin{aligned} \text{Im } \sigma_{xy, \varsigma}^{\lambda\nu\lambda'v'}(\omega) &= \varsigma \int_0^\infty dk \frac{e^2 a^4 t^4 k^3 (p^2 - r^2)}{2\hbar^3 \omega \hbar^{\lambda\nu} \hbar^{\lambda'v'}} \\ &\times [f(\varepsilon_{k, \lambda\nu}) - f(\varepsilon_{k, \lambda\nu} + \hbar\omega)] \\ &\times \delta[\omega - \omega_{\lambda\nu}^{\lambda'v'}(k)], \end{aligned}$$

where the integral of $\cos(2\phi)$ and $\sin(2\phi)$ over the angle ϕ is zero in Eqs. (8) and (9), respectively, and $\omega_{\lambda\nu}^{\lambda'v'}(k) = (\varepsilon_{k, \lambda'v'} - \varepsilon_{k, \lambda\nu})/\hbar$ is the energy spacing frequency between the initial and final states.

The total optical conductivity of the system is the summation of the contributions at the two valleys,

$$\sigma_{\alpha\beta}(\omega) = \sum_{\varsigma=\pm} \sigma_{\alpha\beta}^\varsigma(\omega). \quad (13)$$

Equation (11) shows that the real part of the longitudinal optical conductivity is the same for both valleys. This means that we can write the real part as $\text{Re } \sigma_{xx}(\omega) = g_v \text{Re } \sigma_{xx}^{\zeta}(\omega)$ with the valley degeneracy factor $g_v = 2$. For the imaginary part, Eq. (12) shows that the system is valley antisymmetric with respect to a change in sign of ζ , i.e., $\text{Im } \sigma_{xy, +}^{\lambda\nu\lambda'\nu'}(\omega) = -\text{Im } \sigma_{xy, -}^{\lambda\nu\lambda'\nu'}(\omega)$. This means that the imaginary part of the Hall conductivity vanishes because the contributions from the two valleys cancel each other out.

The absorption of incoming linearly polarized radiation is given by the real part of the longitudinal conductivity. For finite frequency the optical response to circularly polarized radiation with right-handed (+) and left-handed (-) polarizations, the absorptive part of the optical conductivity under circular polarized radiation at valley ζ can be found as [16]

$$\text{Re } \sigma_{\pm}^{\zeta}(\omega) = \text{Re } \sigma_{xx}^{\zeta}(\omega) \mp \text{Im } \sigma_{xy}^{\zeta}(\omega). \quad (14)$$

Therefore, in order to calculate the amount of absorbed radiation, we only need to calculate the real part of the longitudinal conductivity as presented in Eq. (11) and the imaginary part of the Hall conductivity as given by Eq. (12).

IV. RESULTS AND DISCUSSION

In this study, we consider both n -type and p -type ML-MoS₂ in the presence of a relatively weak infrared or terahertz radiation field, such that the linear response theory used in this paper is valid [47,52], and that the electron or hole density do not change significantly. This is because the large band gap suppresses the photoexcited electron-hole pairs. This means that only the electronic transitions within the valence or conduction band are included in the present study (i.e., $\lambda = \lambda'$). The chemical potential μ_{λ} for electrons in n -type and holes in p -type ML-MoS₂ can be determined, respectively, through the conservation of carrier numbers

$$n_e = g_v \sum_{\lambda=+,v=\pm} \sum_{\mathbf{k}} f(\varepsilon_{\mathbf{k},\lambda\nu}) \quad (15)$$

and

$$n_h = g_v \sum_{\lambda=-,v=\pm} \sum_{\mathbf{k}} [1 - f(\varepsilon_{\mathbf{k},\lambda\nu})]. \quad (16)$$

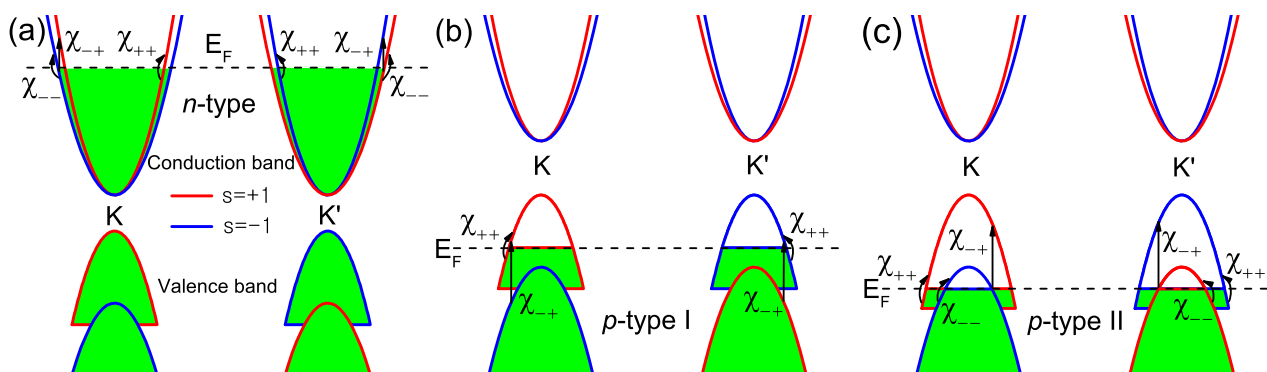


FIG. 1. Schematic presentation of the band structure and the possible optical transition channels in both valleys for n -type in (a) and p -type I in (b) in ML-MoS₂ with the Fermi level E_F between the two top points of spin-split valence subbands. In (c), p -type II ML-MoS₂ with Fermi energy E_F for holes below the top point of $\nu = -$ valence subband. The possible optical absorption channels are indicated by $\chi_{\nu\nu'}$.

To perform numerical calculations for the optical conductivity, we take the spin relaxation time for electrons $\tau_{\text{spin}}^e = 3$ ps and for holes $\tau_{\text{spin}}^h = 200$ ps for spin-flip transitions [53]. The free carrier energy relaxation time is about $\tau_c = 0.5$ ps for spin-conserving intraband transitions [54]. Using the energy relaxation approximation, this allows us to replace the $\delta(E)$ functions in Eqs. (11) and (12) with a Lorentzian distribution: $\delta(E) \rightarrow (E_\tau/\pi)/(E^2 + E_\tau^2)$, where $E_\tau = \hbar/\tau$ is the width of the distribution [55]. It should be noted that energy relaxation time is a frequency-dependent parameter and is usually set to a constant for numerical calculation [56]. The optical conductivities in Eqs. (11) and (12) are evaluating numerically by the standard Gauss-Kronrod quadrature method for one-dimensional integrals [57] and the integrals converge naturally due to the presence of the Fermi-Dirac function and the Lorentzian distribution of the energy conservation Delta function.

In Fig. 1, we show the low-energy electronic band structure and corresponding optical transitions channels $\chi_{\nu\nu'}$ for ML-MoS₂ at K and K' valleys. In ML-MoS₂, the intrinsic SOC causes a minor spin split in the conduction band, but it induces a large spin split in the valence band as shown in Fig. 1. Furthermore, the spin-up and spin-down components are completely decoupled, which makes electronic transitions between opposite spin subbands impossible. Upon inclusion of the Rashba effect, the energy spectrum is only slightly affected, but it mixes the spin states and, therefore, the electronic transitions between spin split subbands as shown in Fig. 1 become possible. Because of the absolute value of the longitudinal/Hall optical conductivity is valley-independent as we have discussed in the previous section, we use the symbol $\chi_{\nu\nu'}$ to represent optical transitions from ν to ν' . We denote the spin-resolved bands that are lower in energy by $\nu = -$ and the higher energy bands by $\nu = +$.

ML-MoS₂ is a semiconductor which can be doped through techniques such as chemical doping or applying a gate voltage [9,60]. If the system is electron doped, i.e., n -type ML-MoS₂, the optical conductivity can be separated into the contributions stemming from spin-conserving and spin-flip transitions within the conduction band. Therefore, the conductivity is the summation over the contributions from the optical transition channels as shown in Fig. 1(a). Thanks to the large spin split at the top of the valence band, the optical

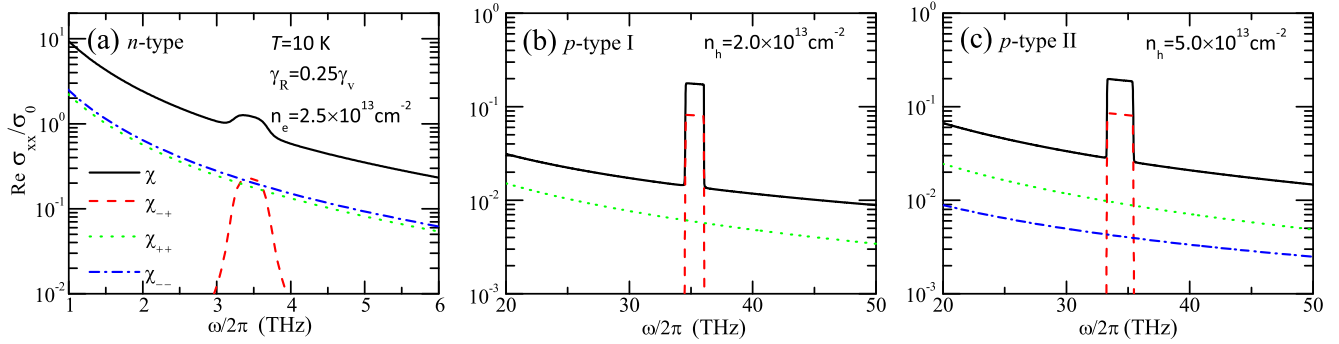


FIG. 2. Finite-temperature contributions from different transition channels to the real part of the longitudinal optical conductivity for different doping types and concentrations as indicated. The contributions to the optical conductivity marked in (a)–(c) correspond to the transition channels shown in Fig. 1 and the black solid curve presented by χ is the summation of all the transition channels. Here, $\sigma_0 = e^2/(4\hbar)$.

transition channels depend strongly on the doping level in p -type samples. For low p -type doping, the energy lower valence spin-split subband is fully occupied with electrons. Therefore, free carrier absorption is forbidden for this subband as shown in Fig. 1(b). If the p -type doping is larger, the subband can contribute to intraband transitions as indicated in Fig. 1(c). In order to determine the optical absorption, one needs to calculate the real part of the optical conductivity as outlined in the previous section. As a consequence, measuring the optical absorption for different doping levels allows us to determine the conductivity as defined in Eqs. (13) and (14).

In Fig. 2, we show the contributions from different electronic transition channels to optical conductivity at a fixed electron density n_e for n -type ML-MoS₂ and with fixed hole density n_h for p -type I/II ML-MoS₂ at $T = 10$ K with $\gamma_R = 0.25\gamma_v$. We see that the optical conductivity of n -type (p -type) ML-MoS₂ has contributions from both spin-conserving and spin-flip transitions as indicated by the electronic transition channels in Fig. 1. Due to symmetric dispersion relation at K and K' valleys, the contributions to the optical conductivity in different valleys in Fig. 2 are identical to each other except for the fact that the bands have opposite spin indices for the higher and lower energy bands, respectively. In Fig. 2(b), free carrier absorption only exists in the highest spin-resolved subband because the lowest subband is fully occupied as shown in Fig. 1(b). Therefore, the intraband transitions in p -type II ML-MoS₂ contribute more to the optical conductivity than its p -type I counterpart. This can be clearly seen in Figs. 2(b) and 2(c). We also notice that the contributions to the optical conductivity via free carrier absorption within the $\nu = +$ subband are larger than that within the $\nu = -$ subband for p -type sample and it is opposite for n -type sample. For intraband transitions, which mainly occur in a small low-frequency range, the relaxation time does not vary strongly with frequency. It is shown that the frequency dependence of the free carrier relaxation time in InP depends very little on frequency in the low-frequency range [58]. At the same time, the Rashba effect will also not affect the free carrier relaxation time a lot because the Rashba effect almost does not involve the intraband scattering mechanism. Usually, the Drude model with a single relaxation time describes very well the intraband optical conductivity [59].

Spin-conserving intraband transitions give rise to low-frequency THz absorption, whereas spin-flip transitions result

in a wide absorption peak as shown in Fig. 2(a) and a roughly rectangularly shaped spectral absorption as presented in Figs. 2(b) and 2(c). In Fig. 2(a), the total optical conductivity has a wide absorption peak in the low-radiation frequency and the total optical conductivity increases at low radiation frequency which shows the usual Drude-like behavior. The wide absorption peak is in the frequency regime 3–3.8 THz which is due to the small spin splitting in the conduction band. The absorption peak shape is due to the smaller energy scale of the transitions in the n -type sample. In Figs. 2(b) and 2(c), the total optical conductivity has an absorption window in the high-frequency regime and increases at low radiation frequency as well, while the roughly rectangularly shaped absorption windows in Figs. 2(b) and 2(c) is in the frequency regimes 34.5–36 THz and 33.3–35.5 THz which are induced by the larger spin splitting in the valence band.

In Fig. 3 we show the contributions to the optical absorption of circularly and linearly polarized light field in the two valleys. The optical conductivity consists of a Drude-like part induced by the contribution from intraband transitions that conserve spin, and a narrow absorption window due to spin-flip transitions. Under the linearly and circularly polarized light radiation, the Drude-like part is the same because the contributions to the imaginary part of the Hall conductivity are zero for intraband transitions, which can be seen in Eq. (9). As explained in Sec. III, the absorption of light with linear polarization is proportional to the longitudinal conductivity $\text{Re}\sigma_{xx}^{\zeta}$, which is the same for both valleys. However, the absorption of circularly polarized light is also affected by the imaginary part of the Hall conductivity $\text{Im}\sigma_{xy}^{\zeta}$ which is \pm opposite for both valleys. As a consequence, the absorption of circularly polarized light is valley-dependent. For the total response to left and right handed circularly polarized light as a function of radiation frequency, σ_{-} probes mainly the K valley and σ_{+} the K' one. Additionally, their average is equal to the longitudinal optical conductivity. These interesting findings agree with the results for silicene [55].

The optical conductivity of n - and p -type II ML-MoS₂ is shown in Fig. 4 as a function of radiation frequency at fixed carrier density and γ_R for different temperatures. For $\gamma_R = 0.25\gamma_v$ and $T = 10$ K, the p -type doped sample could be regarded as p -type I when the hole density $n_h < 3.36 \times 10^{13} \text{ cm}^{-2}$ and becomes p -type II when $n_h > 3.36 \times 10^{13} \text{ cm}^{-2}$. In Fig. 4(a), we find that the strength of the wide

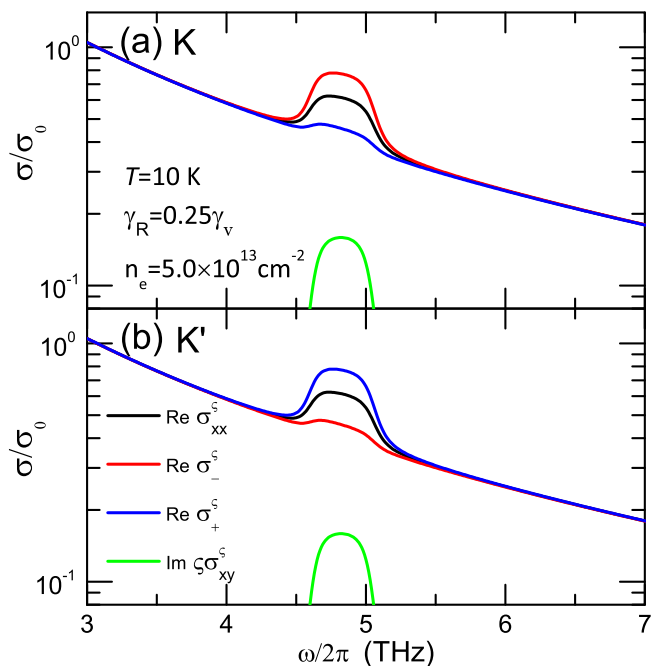


FIG. 3. The absorption part of the optical conductivity to circularly polarized radiation of n -type ML-MoS₂ at temperature $T = 10$ K for electron density $n_e = 5 \times 10^{13} \text{ cm}^{-2}$ and Rashba parameter $\gamma_R = 0.25\gamma_v$. The results are shown for (a) the K valley and (b) the K' valley.

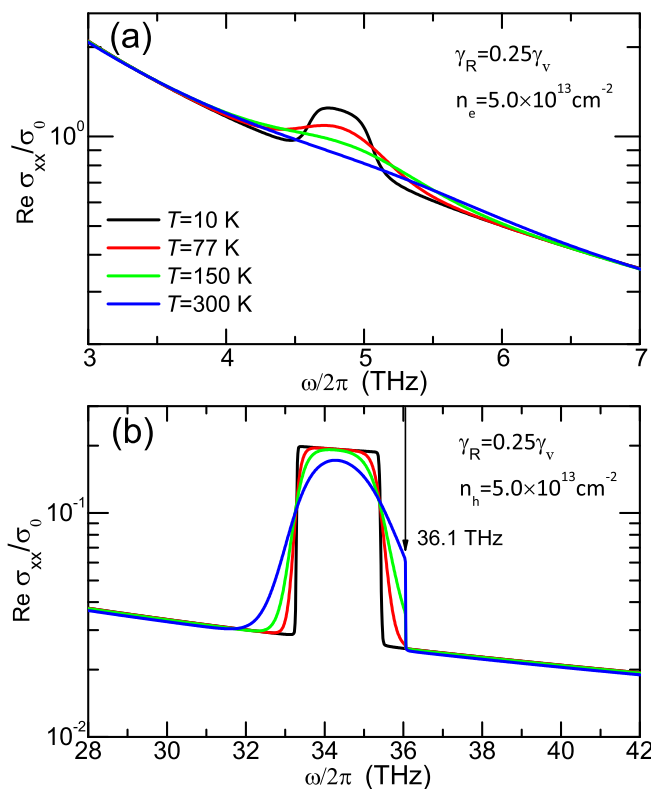


FIG. 4. The real part of the longitudinal optical conductivity as a function of radiation frequency at a fixed carrier density (a) for n -type and (b) for p -type ML-MoS₂ for different temperatures.

absorption peak decreases with increasing temperature and vanishes at room temperature. The optical conductivity in Fig. 4(b) has an absorption peak at room temperature and an absorption window at low temperature. At low temperature, $T = 10$ K, there is a sharper cutoff in absorption window edges. We notice that a hard cutoff at 36.1 THz always exists for the high-temperature cases. With higher temperatures, the electrons in the case of Fig. 1(c) redistribute their states above the Fermi level due to the smoothing of the Fermi-Dirac distribution. Thus, electrons can occupy some states in the top of the $\nu = -$ subband and electronic transitions from the $\nu = -$ subband to the $\nu = +$ subband are possible. However, the top points of the two subbands in the valence band have an energy spacing corresponding to a radiation frequency of 36.1 THz for $\gamma_R = 0.25\gamma_v$. Thus, 36.1 THz is the largest optical transition frequency that allows for spin-flip transitions. The Drude-like part of the optical conductivity does not show much difference for different temperatures because the same energy relaxation scattering time is used in the calculation. Generally, we can obtain a stronger absorption peak and a sharper absorption window in the conductivity spectrum at lower temperature. However, the spin-flip transition induced absorption in the p -type sample can still be observed at room temperature.

In Fig. 5, we show the optical conductivity of n - and p -type ML-MoS₂ as a function of radiation frequency for the fixed $\gamma_R = 0.25\gamma_v$ and $T = 10$ K for different carrier densities. For ML-MoS₂, n - and p -type doping samples can be realized through the field effect with different source and drain

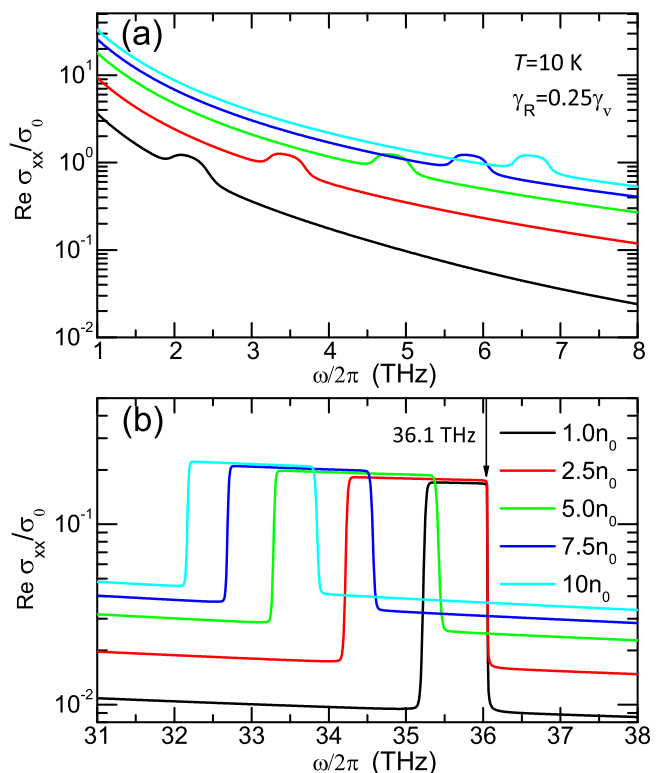


FIG. 5. The real part of the longitudinal optical conductivity as a function of radiation frequency for $\gamma_R = 0.25\gamma_v$ and $T = 10$ K and different carrier densities where $n_0 = 1 \times 10^{13} \text{ cm}^{-2}$. The results are shown for (a) n -type and (b) p -type ML-MoS₂.

contacts [9,61] and the doping levels can be tuned through the application of a gate voltage. Usually, one could reach high carrier densities [9,62] and we choose the carrier densities with a magnitude of 10^{13} cm^{-2} in our calculations. As can be seen in Fig. 5, the contribution to the optical conductivity from intraband transitions increases with increasing carrier density in both n - and p -type samples. More interestingly, we find that the wide absorption peak in Fig. 5(a) blueshifts to higher frequencies and the absorption window in Fig. 5(b) redshifts to lower frequencies with increasing carrier density. At the fixed Rashba parameter and temperature, the chemical potential for electrons/holes in n -/ p -type samples increases/decreases with increasing carrier density. As a result, the energy required for direct spin-flip transitions increases/decreases with increasing electron/hole density in n -/ p -type ML-MoS₂ due to the Pauli blockade effect [63]. This is how the blueshifts of the absorption peak in the n -type sample and the redshifts of the absorption window in the p -type sample can occur. In Fig. 5(b), we see that the right boundary of the absorption windows at position 36.1 THz is the largest optical transition frequency for those cases. Apart from the contribution of intraband transitions, we also find that the strength of the absorption peak in n -type samples and the height of the absorption window in p -type samples is slightly affected by the carrier density. Besides, the width of the absorption peak in the n -type sample varies slightly with electron density and the width of the absorption window in the p -type sample varies distinctly with changing hole density. These theoretical results show that the optical absorption of ML-MoS₂ in the THz and infrared regimes can be effectively tuned by varying the carrier density.

In Fig. 6, we plot the low-energy band structure and the energy spacing of spin-split subbands in conduction and

valence bands of ML-MoS₂ as a function of wave vector at the K valley in the presence of the Rashba effect with different Rashba parameters. Usually, the Rashba SOC strength in semiconductors can be tuned by an electric field [22–24]. In Fig. 6(b), near the K point, the energy spacing between two spin-orbit split conduction subbands increases with increasing wave vector or Rashba parameter. With increasing γ_R , the energy spacing turns from a roughly parabolic curve to a roughly linear line and a spin-orbit split gap can be observed at $ka = 0$ for large γ_R . In Fig. 6(c), one can see that the energy spacing between two-spin split valence subbands decreases with increasing wave vector when $\gamma_R = 0.1\gamma_v, 0.25\gamma_v$, and $0.5\gamma_v$. When $\gamma_R = 0.75\gamma_v$, the energy spacing of spin-split subbands first increases then decreases slightly with increasing wave vector, whereas for $\gamma_R = \gamma_v$, the energy spacing of the subbands increases with increasing wave vector. We find that the band structure of ML-MoS₂ can be fine-tuned by the Rashba effect and a more complicated band structure of spin-split subbands with different Rashba parameters can be found in the valence bands.

The optical conductivity of n - and p -type ML-MoS₂ is shown in Fig. 7 as a function of radiation frequency at the fixed temperature and carrier density for different Rashba parameters. At large carrier density (e.g., $5 \times 10^{13} \text{ cm}^{-2}$), we find that the top point of the $\nu = -$ valence subband and the chemical potential of electrons/holes in n -/ p -type ML-MoS₂ do not vary with changing γ_R . Thus, for a p -type ML-MoS₂ with a hole density $n_h = 5 \times 10^{13} \text{ cm}^{-2}$, it can be always regarded as p -type II for different γ_R . With large carrier density, we find that the dependence of the Fermi level on the Rashba parameter is negligible. With low carrier density, we find that the Fermi level first stays the same with low Rashba

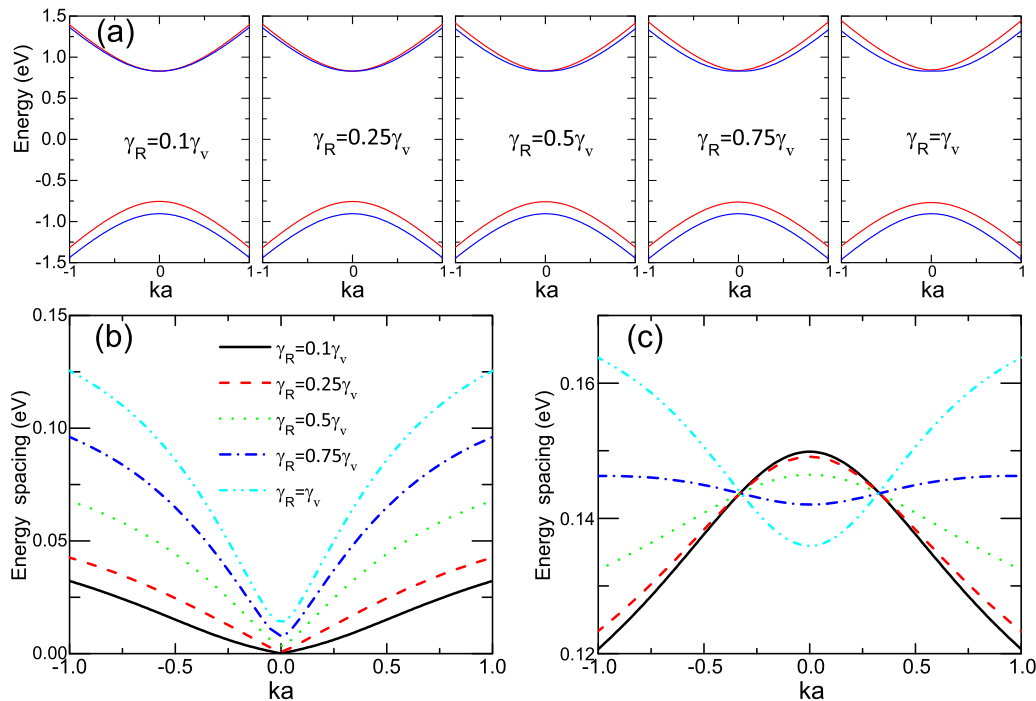


FIG. 6. (a) Low-energy effective band structure of ML-MoS₂ at K valley with different γ_R . The spin-up ($s = 1$) and spin-down ($s = -1$) subbands are denoted by red and blue solid curves, respectively. The energy spacing between two spin-split subbands with different γ_R is shown for (b) conduction band and (c) valence band.

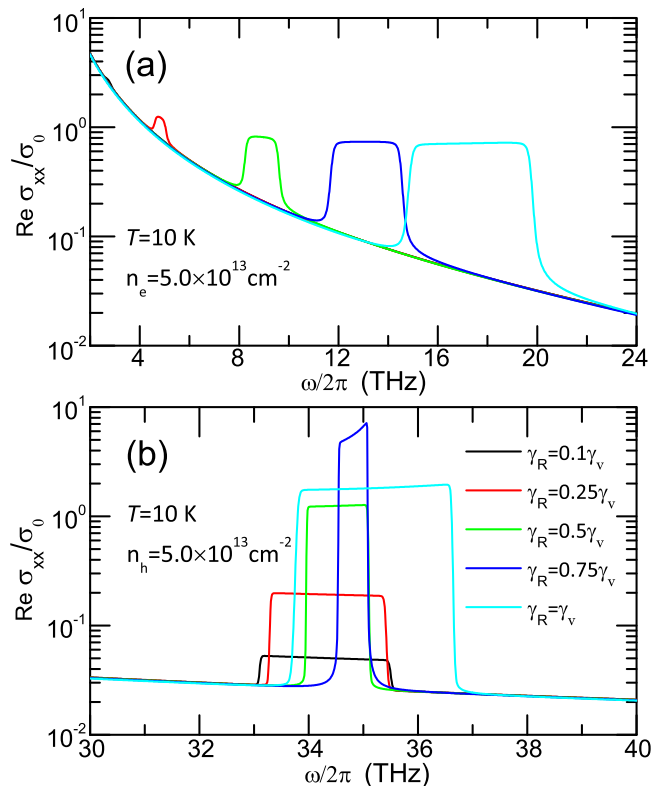


FIG. 7. The real part of the optical conductivity as a function of radiation frequency at fixed temperature $T = 10$ K and carrier density $5 \times 10^{13} \text{ cm}^{-2}$ for different Rashba spin-orbit parameters. The results are shown for (a) n -type ML-MoS₂ and (b) p -type II ML-MoS₂.

coupling strength and then decreases slightly with increasing Rashba coupling strength in the n -type sample, while in the low-density p -type sample, the Fermi level always decreases slightly with increasing γ_R .

In Figs. 7(a) and 7(b), we see that the Drude-like part of the optical conductivity in n/p -type ML-MoS₂ is not affected by the value of γ_R . The wide absorption peak in Fig. 7(a) blueshifts and the shape of it turns into an absorption window with increasing γ_R . At the same time, the width of the absorption window increases with increasing γ_R and the height of the absorption window varies slightly. In Fig. 7(b), we can see that there are also absorption windows in the optical conductivity curve with different Rashba parameters but the width and height of them vary a lot with changing γ_R . Through the five sets of data plotted in Fig. 7(b), we find that the widest absorption window can be obtained when $\gamma_R = \gamma_v$ and the narrowest absorption window is found when $\gamma_R = 0.75\gamma_v$. This feature can be derived from Fig. 6(c). We see that the boundaries of these absorption windows in Fig. 7(b) do not match the energy spacings between two spin-split valence subbands at $ka = 0$ in Fig. 6(c). That means that the boundaries of spin-flip transitions are mainly delimited by the holes' optical transitions near the Fermi level limited by the Fermi-Dirac distribution in the case of a large hole density and low temperature. When $\gamma_R = 0.75\gamma_v$, the narrow region of energy spacing in Fig. 6(c) results in the narrowest absorption window in Fig. 7(b) and a blade shape can be seen at the top of the absorption window.

Additionally, the dispersion relation for spin-split conduction subbands in ML-MoS₂ is similar to a traditional 2DEG system in the presence of the Rashba effect. Thus, the results in Fig. 7(a) show some similarities with traditional 2DEGs [27,28]. Due to the complexity of spin-orbit split valence subbands, the height of the absorption windows in Fig. 7(b) varies a lot with changing Rashba parameter which is different from that of traditional 2D systems. As a conclusion, we can say that the optoelectronic properties of ML-MoS₂ with different doping types can be effectively tuned by the Rashba effect.

In order to understand the peculiar phenomenon that the height of the absorption window of a p -type sample in the presence of the Rashba effect varies a lot with changing Rashba parameter, we would like to examine the role that the intrinsic SOC plays. Although the intrinsic SOC parameter γ_v is a constant that cannot be changed by external field, we would like to show how the intrinsic SOC decides the optical property of ML-MoS₂ by choosing different intrinsic SOC parameters. In Fig. 8, we plot the contributions of the spin-flip transitions to the optical conductivity of n - and p -type ML-MoS₂ as a function of radiation frequency at fixed temperature and carrier density. Here, we redefine γ'_v as the intrinsic SOC parameter. Figure 8(a) shows the spin-flip optical conductivity part of Fig. 7(a). With small Rashba coupling strength, we see that the spin-flip contribution of electrons in the n -type system decreases both in width and in height as the coupling strength decreases. As can be seen from Figs. 8(a)–8(d), the behavior of the optical conductivity with different γ_R is only slightly affected by the intrinsic SOC. The slight difference is caused by the minor modification of the spin split in the conduction band with different γ'_v . From Figs. 8(e)–8(h), we find the following features: (i) With large intrinsic SOC (e.g., $\gamma'_v = 75$ meV, 37.5 meV), the height of the absorption window varies strongly with the Rashba parameter. (ii) The heights of the absorption windows change slightly and the shapes of these curves approach those for the n -type case with a small γ'_v . (iii) In the absence of intrinsic SOC ($\gamma'_v = 0$ meV), the optical conductivity curves in Fig. 8(h) are almost identical to those in Fig. 8(d). The ultrafine difference is due to the different scattering times for electrons and holes chosen in our calculation. Indeed, the frequency and Rashba effect would also affect the relaxation time for the interband transitions. As can be seen in Figs. 8(d) and 8(h), the relaxation times used in the energy relaxation approximation only slightly affect the two boundaries of the absorption window and do not affect much the total spin-flip optical conductivity curve. With larger relaxation scattering time which means smaller broadening of scattering states, the spin-flip optical conductivity will approach the result for the long-wavelength optical limit. In this study, we are more interested in the spin-flip transition absorption part which is in the high-frequency regime where the contribution of intraband transitions is weak. Thus, we may safely assume that the energy relaxation time used in the numerical calculation is reliable for describing the optical absorption in the frequency range considered in this study. Therefore, we can see that the intrinsic SOC plays an important role in affecting the optical absorption spectrum of p -type ML-MoS₂ for changing Rashba SOC strength. In monolayer MX₂, the intrinsic SOC and the other parameters in Eq. (1)

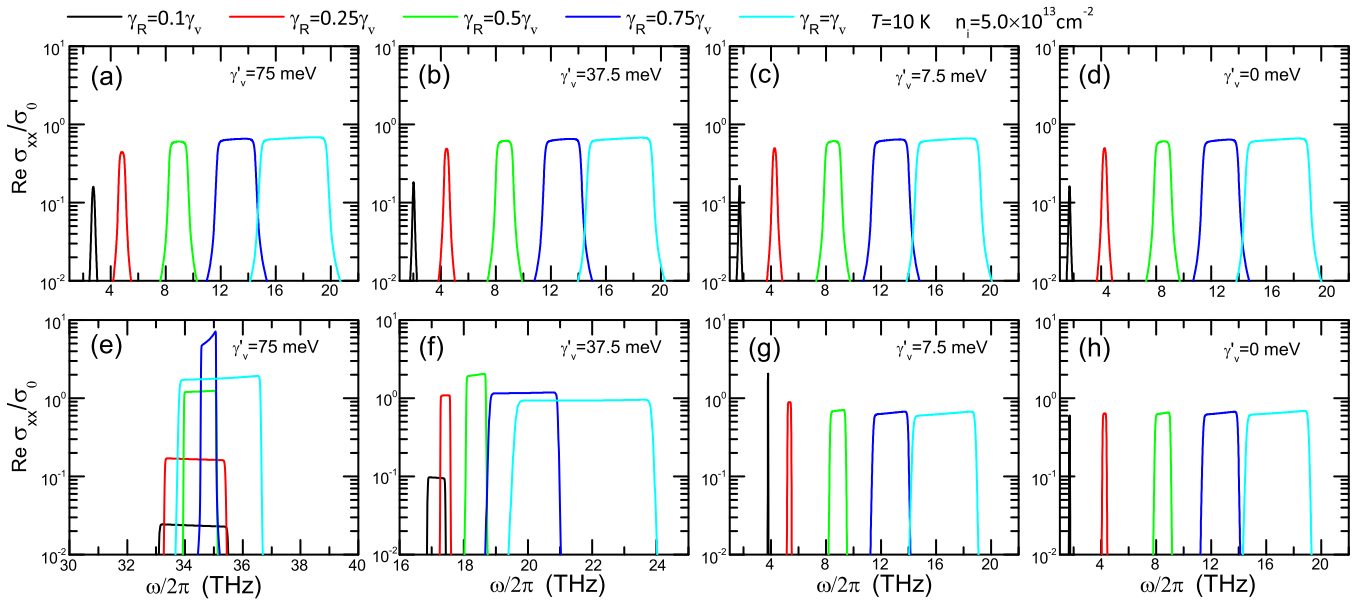


FIG. 8. The real part of the longitudinal optical conductivity contributed from the spin-flip transitions as a function of radiation frequency at fixed temperature and carrier density for different Rashba parameters. Here we use γ'_v to replace γ_v as the intrinsic SOC parameter. The results for different γ'_v are shown for (a)–(d) *n*-type and (e)–(h) *p*-type samples.

vary with different compounds of M and X. Thus, the infrared to THz optical absorption windows with different bandwidths ranges and shapes can also be observed in other ML-TMDC materials in the presence of the Rashba effect.

V. CONCLUSIONS

In this study, we have investigated the infrared to terahertz optoelectronic properties of *n*- and *p*-type ML-MoS₂ in the presence of the Rashba effect. The optical conductivity is evaluated using the standard Kubo formula. The effects of the polarization of the radiation field, temperature, carrier density, and Rashba parameter on the optical conductivity have been examined. The total optical conductivity contains contributions from different transition channels between different spin states. We have also examined the role that the intrinsic SOC plays in affecting the optoelectronic properties of ML-MoS₂ in the presence of the Rashba effect. The main conclusions we have obtained from this study are summarized as follows.

In ML-MoS₂, free carrier absorption exists in the entire infrared to terahertz regime. Spin-flip transitions induce wide absorption peaks and absorption windows which range from infrared to THz. Free carrier absorption is weakly affected by the polarization direction of the radiation, temperature, and Rashba parameter but depends strongly on the carrier density. Under circularly polarized radiation, the spin-flip transitions induce a valley-selective absorption. However, the summation over them is the same as the longitudinal optical conductivity.

A stronger absorption peak or sharper absorption window can be observed at lower temperature. The position and width of the absorption peak and absorption window can be effectively tuned by carrier density and Rashba parameter. This suggests that ML-MoS₂ has a wide tunable optical response in the infrared to THz radiation regime.

In the presence of the Rashba effect, the features of optical conductivity in *n*-type ML-MoS₂ are similar to those in 2DEGs and the intrinsic SOC has a strong influence on the optoelectronic property of *p*-type ML-MoS₂.

We have found that the optoelectronic properties of *n*- and *p*-type ML-MoS₂ can be effectively tuned by the carrier density and Rashba parameter which makes ML-MoS₂ a promising infrared and THz material for optics and optoelectronics. The obtained theoretical findings can be helpful for understanding of the optical properties of ML-MoS₂. We hope the theoretical predictions in this paper can be verified experimentally.

ACKNOWLEDGMENTS

Y.M.X. acknowledges financial support from the China Scholarship Council (CSC). This work was also supported by the National Natural Science Foundation of China (Grant No. 11574319), Ministry of Science and Technology of China (Grant No. 2011YQ130018), Department of Science and Technology of Yunnan Province, and by the Chinese Academy of Sciences. B.V.D. is supported by a Ph.D. fellowship from the Flemish Science Foundation.

[1] K. S. Novoselov, A. K. Geim, S. V. Morozov, D. Jiang, Y. Zhang, S. V. Dubonos, I. V. Grigorieva, and A. A. Firsov, *Science* **306**, 666 (2004).

[2] Q. H. Wang, K. Kalantar-Zadeh, A. Kis, J. N. Coleman, and M. S. Strano, *Nat. Nanotechnol.* **7**, 699 (2012).

- [3] K. F. Mak, C. Lee, J. Hone, J. Shan, and T. F. Heinz, *Phys. Rev. Lett.* **105**, 136805 (2010).
- [4] Zhiming M. Wang, *MoS₂: Materials, Physics, and Devices* (Springer, Switzerland, 2014).
- [5] A. Splendiani, L. Sun, Y. Zhang, T. Li, J. Kim, C.-Y. Chim, G. Galli, and F. Wang, *Nano Lett.* **10**, 1271 (2010).
- [6] C. Lee, H. Yan, L. E. Brus, T. F. Heinz, J. Hone, and S. Ryu, *ACS Nano* **4**, 2695 (2010).
- [7] B. Radisavljevic, M. B. Whitwick, and A. Kis, *ACS Nano* **5**, 9934 (2011).
- [8] B. Radisavljevic, A. Radenovic, J. Brivio, V. Giacometti, and A. Kis, *Nat. Nanotechnol.* **6**, 147 (2011).
- [9] B. Radisavljevic and A. Kis, *Nat. Mater.* **12**, 815 (2013).
- [10] H. Li, Z. Yin, Q. He, H. Li, X. Huang, G. Lu, D. W. H. Fam, A. I. Y. Tok, Q. Zhang, and H. Zhang, *Small* **8**, 63 (2012).
- [11] Z. Yin, H. Li, H. Li, L. Jiang, Y. Shi, Y. Sun, G. Lu, Q. Zhang, X. Chen, and H. Zhang, *ACS Nano* **6**, 74 (2012).
- [12] R. S. Sundaram, M. Engel, A. Lombardo, R. Krupke, A. C. Ferrari, Ph. Avouris, and M. Steiner, *Nano Lett.* **13**, 1416 (2013).
- [13] D. Xiao, G.-B. Liu, W. Feng, X. Xu, and W. Yao, *Phys. Rev. Lett.* **108**, 196802 (2012).
- [14] A. Kormányos, V. Zólyomi, N. D. Drummond, P. Rakyta, G. Burkard, and V. I. Fal'ko, *Phys. Rev. B* **88**, 045416 (2013).
- [15] H.-Z. Lu, W. Yao, D. Xiao, and S.-Q. Shen, *Phys. Rev. Lett.* **110**, 016806 (2013).
- [16] Z. Li and J. P. Carbotte, *Phys. Rev. B* **86**, 205425 (2012).
- [17] A. Scholz, T. Stauber, and J. Schliemann, *Phys. Rev. B* **88**, 035135 (2013).
- [18] R. Ganatra and Q. Zhang, *ACS Nano* **8**, 4074 (2014).
- [19] K. F. Mak, K. He, J. Shan, and T. F. Heinz, *Nat. Nanotechnol.* **7**, 494 (2012).
- [20] H. Zeng, J. Dai, W. Yao, D. Xiao, and X. Cui, *Nat. Nanotechnol.* **7**, 490 (2012).
- [21] T. Cao, G. Wang, W. Han, H. Ye, C. Zhu, J. Shi, Q. Niu, P. Tan, E. Wang, B. Liu, and J. Feng, *Nat. Commun.* **3**, 887 (2012).
- [22] S. Datta and B. Das, *Appl. Phys. Lett.* **56**, 665 (1990).
- [23] M. M. Glazov, E. Ya. Sherman, and V. K. Dugaev, *Physica E* **42**, 2157 (2010).
- [24] M. W. Wu, J. H. Jiang, and M. Q. Weng, *Phys. Rep.* **493**, 61 (2010).
- [25] W. Xu, *Appl. Phys. Lett.* **82**, 724 (2003).
- [26] X. F. Wang, *Phys. Rev. B* **72**, 085317 (2005).
- [27] D. W. Yuan, W. Xu, Z. Zeng, and F. Lu, *Phys. Rev. B* **72**, 033320 (2005); C. H. Yang, W. Xu, Z. Zeng, F. Lu, and C. Zhang, *ibid.* **74**, 075321 (2006).
- [28] Y. S. Ang, J. C. Cao, and C. Zhang, *Eur. Phys. J. B* **87**, 28 (2014).
- [29] J. Ibañez-Azpiroz, A. Eiguren, E. Ya. Sherman, and A. Bergara, *Phys. Rev. Lett.* **109**, 156401 (2012).
- [30] J. Ibañez-Azpiroz, A. Bergara, E. Ya. Sherman, and A. Eiguren, *Phys. Rev. B* **88**, 125404 (2013).
- [31] C. L. Kane and E. J. Mele, *Phys. Rev. Lett.* **95**, 226801 (2005).
- [32] H. Ochoa and R. Roldán, *Phys. Rev. B* **87**, 245421 (2013).
- [33] J. Klinovaja and D. Loss, *Phys. Rev. B* **88**, 075404 (2013).
- [34] D. Marchenko, A. Varykhalov, M. R. Scholz, G. Bihlmayer, E. I. Rashba, A. Rybkin, A. M. Shikin, and O. Rader, *Nat. Commun.* **3**, 1232 (2012).
- [35] P. D. C. King, R. C. Hatch, M. Bianchi, R. Ovsyannikov, C. Lupulescu, G. Landolt, B. Slomski, J. H. Dil, D. Guan, J. L. Mi, E. D. L. Rienks, J. Fink, A. Lindblad, S. Svensson, S. Bao, G. Balakrishnan, B. B. Iversen, J. Osterwalder, W. Eberhardt, F. Baumberger, and Ph. Hofmann, *Phys. Rev. Lett.* **107**, 096802 (2011).
- [36] T. Stauber and J. Schliemann, *New J. Phys.* **11**, 115003 (2009).
- [37] A. Scholz, T. Stauber, and J. Schliemann, *Phys. Rev. B* **86**, 195424 (2012).
- [38] W. Wang, C. Zhang, and Z. Ma, *J. Phys.: Condens. Matter* **24**, 035303 (2012).
- [39] P. Ingenhoven, J. Z. Bernád, U. Zülicke, and R. Egger, *Phys. Rev. B* **81**, 035421 (2010).
- [40] M. M. Perera, M.-W. Lin, H.-J. Chuang, B. P. Chamlagain, C. Wang, X. Tan, M. M.-C. Cheng, D. Tománek, and Z. Zhou, *ACS Nano* **7**, 4449 (2013).
- [41] K. Dolui, I. Rungger, and S. Sanvito, *Phys. Rev. B* **87**, 165402 (2013).
- [42] Z. Y. Zhu, Y. C. Cheng, and U. Schwingenschlögl, *Phys. Rev. B* **84**, 153402 (2011).
- [43] A. Kormányos, V. Zólyomi, N. D. Drummond, and G. Burkard, *Phys. Rev. X* **4**, 011034 (2014).
- [44] A. O. Slobodeniuk and D. M. Basko, *2D Mater.* **3**, 035009 (2016).
- [45] J. Qi, X. Li, Q. Niu, and J. Feng, *Phys. Rev. B* **92**, 121403(R) (2015).
- [46] See, e.g., I. N. Bronshtein, K. A. Semendyayev, G. Musiol, and H. Muehlig, *Handbook of Mathematics* (Springer, Berlin, 2007).
- [47] See, e.g., G. D. Mahan, *Many-Particle Physics* (Kluwer Academic, New York, 2000), p. 165.
- [48] Á. Bácsi and A. Virostek, *Phys. Rev. B* **87**, 125425 (2013).
- [49] See, e.g., M. P. Marder, *Condensed Matter Physics* (Wiley, New York, 2000).
- [50] P. M. Krstajić, P. Vasilopoulos, and M. Tahir, *Phys. Rev. B* **94**, 085413 (2016).
- [51] V. Vargiamidis, P. Vasilopoulos, and G.-Q. Hai, *J. Phys.: Condens. Matter* **26**, 345303 (2014).
- [52] G. F. Giuliani and G. Vignale, *Quantum Theory of the Electron Liquid* (Cambridge University Press, Cambridge, 2005).
- [53] Y. Song and H. Dery, *Phys. Rev. Lett.* **111**, 026601 (2013).
- [54] H. Shi, R. Yan, S. Bertolazzi, J. Brivio, B. Gao, A. Kis, D. Jena, H. G. Xing, and L. Huang, *ACS Nano* **7**, 1072 (2013).
- [55] L. Stille, C. J. Tabert, and E. J. Nicol, *Phys. Rev. B* **86**, 195405 (2012).
- [56] E. J. Nicol and J. P. Carbotte, *Phys. Rev. B* **77**, 155409 (2008).
- [57] R. Piessens, E. de Doncker-Kapenga, C. W. Überhuber, and D. K. Kahaner, *QUADPACK: A Subroutine Package for Automatic Integration* (Springer-Verlag, Berlin, 1983).
- [58] B. Jensen, *J. Appl. Phys.* **50**, 5800 (1979).
- [59] M. Scheffler, M. Dressel, M. Jourdan, and H. Adrian, *Nature (London)* **438**, 1135 (2005).
- [60] H. Liu and P. D. Ye, *Electron Device Lett. IEEE* **33**, 546 (2012).
- [61] S. Chuang, C. Battaglia, A. Azcatl, S. McDonnell, J. S. Kang, X. Yin, M. Tosun, R. Kapadia, H. Fang, R. M. Wallace, and A. Javey, *Nano Lett.* **14**, 1337 (2014).
- [62] N. T. Cuong, M. Otani, and S. Okada, *J. Phys.: Condens. Matter* **26**, 135001 (2014).
- [63] H. J. Krenner, E. C. Clark, T. Nakaoka, M. Bichler, C. Scheurer, G. Abstreiter, and J. J. Finley, *Phys. Rev. Lett.* **97**, 076403 (2006).